Acta Oceanol. Sin., 2018, Vol. 37, No. 1, P. 115–129
DOI: 10.1007/s13131-018-1162-z
http://www.hyxb.org.cn
E-mail: hyxbe@263.net

Assessment of reprocessed sea surface height measurements derived from HY-2A radar altimeter and its application to the observation of 2015–2016 El Niño

JIANG Maofei[1, 2], XU Ke[1]*, LIU Yalong[3], ZHAO Jin[1], WANG Lei[1]

[1] Key Laboratory of Microwave Remote Sensing, National Space Science Center, Chinese Academy of Sciences, Beijing 100190, China

[2] University of Chinese Academy of Sciences, Beijing 100049, China

[3] Yantai Marine Environmental Monitoring Center Station, State Oceanic Administration, Yantai 264000, China

Received 5 June 2017; accepted 13 July 2017

Abstract

Haiyang-2A (HY-2A) is China's first ocean dynamic environment satellite and the radar altimeter is one of its main payloads. One of the main purposes of the radar altimeter is to measure the sea surface height (SSH). The SSH determined from the altimeter range measurements includes some range and geophysical corrections. These corrections largely affect the accuracy of the SSH measurements. The range and the geophysical corrections are reprocessed and the altimeter waveforms in HY-2A sensor interim geophysical data set records (S-IGDR) are retracked from June 1, 2014 to June 14, 2014, and the accuracy of the reprocessed SSH measurements is evaluated. The methods of the range and geophysical corrections used to reprocess HY-2A altimeter data are validated by using these methods to reprocess the Jason-2 range and geophysical corrections and comparing the results with the range and geophysical corrections in Jason-2 geophysical dataset records (GDR) product. A crossover analysis is used to evaluate the accuracy of the reprocessed HY-2A SSH measurements. The standard deviation (STD) of the crossover SSH differences for HY-2A is around 4.53 cm while the STD of the SSH differences between HY-2A and Jason-2 is around 5.22 cm. The performance of the reprocessed HY-2A SSH measurements is significantly improved with respect to the SSH measurements derived from HY-2A interim geophysical dataset records (IGDR) product. The 2015–2016 El Niño has been the strongest El Niño event since 1997–1998. The range and the geophysical corrections in HY-2A IGDR are reprocessed and sea level anomalies are used to monitor the 2015–2016 El Niño. The results show that the HY-2A altimeter can well observe the 2015–2016 El Niño.

Key words: HY-2A, radar altimeter, sea surface height, El Niño

Citation: Jiang Maofei, Xu Ke, Liu Yalong, Zhao Jin, Wang Lei. 2018. Assessment of reprocessed sea surface height measurements derived from HY-2A radar altimeter and its application to the observation of 2015–2016 El Niño. Acta Oceanologica Sinica, 37(1): 115–129, doi: 10.1007/s13131-018-1162-z

1 Introduction

The mean sea level rise, mainly due to the global climate change, has attracted more and more attention. During the past few decades, satellite radar altimetry has become a main tool to observe the global mean sea level change due to its high accuracy and excellent spatial and temporal coverage. The data derived from various satellite altimetry missions play important roles in many science fields, such as ocean circulation, ocean surface topography and climate change (Naenna, 2011).

Haiyang-2A (HY-2A), launched on August 16, 2011, is China's first ocean dynamic environment satellite. It has four payloads: a dual-frequency radar altimeter (Ku and C bands), a microwave scatterometer, a scanning microwave radiometer and a calibration microwave radiometer (Zheng et al., 2014). HY-2A satellite has a scientific and operational requirement to monitor an ocean dynamic environment, including sea surface wind field, sea surface height, significant wave height, sea surface temperature, tides, currents and storms to provide timely disaster and weather forecasting information (Bao et al., 2015). One of the main objectives of the radar altimeter onboard HY-2A satellite is to provide the sea surface height measurements for the studies of marine geoid, tides, currents and sea level rise.

The basic principle of the radar altimeter to measure the sea surface height is straightforward. The radar altimeter transmits an electromagnetic pulse toward the sea surface and receives the pulse reflected from the sea surface (Fu and Cazenave, 2001). By calculating the two-way travel time the pulse takes, we can obtain the range between the satellite and the sea surface. The sea surface height can be obtained by subtracting this range from the orbit height relative to a reference ellipsoid. However, the sea surface height derived from the altimeter range measurements is raw and some range and geophysical corrections should be taken into account. These corrections can largely affect the accuracy of the sea surface height measurements.

Up to now only HY-2A interim geophysical data set records (IGDR) products have been distributed publicly by the National Satellite Ocean Application Service (NSOAS), State Oceanic Administration, China (Peng et al., 2015). The dual-frequency ionosphere correction in the HY-2A IGDR is of poor quality. The dry troposphere correction, model wet troposphere correction, in-

---

*Corresponding author, E-mail: xuke@mirslab.cn verted barometer correction and pole tide correction in the HY-2A IGDR product are invalid after Cycle 76 of HY-2A. These may affect the accuracy assessment of the HY-2A SSH measurements and limit the application of the HY-2A altimeter. Table 1 lists the methods of the range and geophysical corrections applied for HY-2A IGDR and Jason-2 GDR. We can see that some methods of the range and geophysical corrections for HY-2A IGDR are different from those for Jason-2. The dry troposphere correction and model wet troposphere correction in HY-2A IGDR are computed using the data from the National Centers for Environmental Predictions (NCEP) while those in Jason-2 GDR are computed using the data from an operational European Centre for Medium-Range Weather Forecast (ECMWF) atmospheric model. The spatial resolution of the data derived from the NCEP is 1°×1°, which is larger than that (0.12°×0.12°) of the data from the operational ECMWF model. The model ionosphere correction in the HY-2A IGDR is derived from a Bent model while that in Jason-2 GDR is derived from the GPS-derived global ionosphere maps (GIM) model. The sea state bias (SSB) correction in the HY-2A IGDR is derived from a parametric SSB model while that in the Jason-2 GDR is derived from a nonparametric SSB model. The geocentric ocean tide corrections in the HY-2A IGDR are computed using a GOT00.2 tide model, which is relatively old with respect to the GOT4.8 used for the Jason-2 GDR. The dynamic atmosphere correction in the Jason-2 GDR contains the inverted barometer correction and the high frequency wind and pressure correction while the high frequency wind and pressure correction in the HY-2A IGDR is invalid. Therefore, the quality of the HY-2A altimeter data can be further improved and it is of significance to obtain a higher accuracy of the SSH measurements.

Table 1. Comparison of methods of the range and geophysical corrections for HY-2A IGDR, Jason-2 GDR and reprocessed HY-2A data

	HY-2A IGDR	Jason-2 GDR	Reprocessed HY-2A data
Dry troposphere correction	NCEP model	ECMWF model	ERA-Interim model
Wet troposphere correction	ACMR; NCEP model	AMR; ECMWF model	ACMR; ERA-Interim model
Ionospheric correction	dual frequency correction; Bent model	dual frequency correction; GIM model	improved dual frequency correction (Jiang et al., 2017); GIM model
Sea state bias correction	Parametric model (Gaspar et al., 1994);	2-D nonparametric model (Tran, Labroue et al., 2010; Tran, Vandmark et al., 2010);	3-D nonparametric model (Jiang et al., 2016);
Geocentric ocean tide correction	GOT00.2 model; FES2004 model	GOT4.8 model; FES2004 model	GOT4.10 model
Solid earth tide correction	(Cartwright and Edden, 1973)	(Cartwright and Edden, 1973)	(Cartwright and Edden, 1973)
Pole tide correction	(Wahr, 1985)	(Wahr, 1985)	(Wahr, 1985)
Dynamical atmospheric correction	inverted barometer correction	inverted barometer correction plus high frequency wind and pressure correction	DAC from AVISO

In this paper, we aim at achieving three goals. First, improving the quality of the HY-2A altimeter data by reprocessing the range and geophysical corrections in the HY-2A S-IGDR and IGDR, and retracking the altimeter waveforms in the HY-2A S-IGDR. Second, assessing the overall performance of the HY-2A altimeter system using the reprocessed HY-2A SSH data. Third, observing the 2015–2016 El Niño using the reprocessed HY-2A IGDR data.

Unlike the IGDR, the HY-2A S-IGDR has the altimeter waveforms. We retracked the altimeter waveforms using a new MLE4 algorithm (Wang et al., 2013a, b) to derive the range between the satellite and the sea surface. In Table 1, we also list the methods of the range and geophysical corrections we used to reprocess the HY-2A altimeter data. We used the data from ECMWF reanalysis ERA-Interim to compute the dry troposphere correction and the model wet troposphere correction. ERA-interim provides better dry and wet troposphere corrections for the altimeter sea level at climate scales with respect to the operational ECMWF atmospheric model (Legeais et al., 2014; Carrère et al., 2016), and has been applied to the climate change Initiative (CCI) project (Ablain et al., 2015). We improved the HY-2A dual-frequency ionosphere correction by correcting the C-band time tag bias of the HY-2A altimeter with the method described by Jiang et al. (2017). Similar to the Jason-2 GDR, we also computed the model ionosphere correction using the GIM model. We computed the sea state bias correction using a three-dimensional (3-D) nonparametric SSB model developed by Jiang et al. (2016). The geocentric ocean tide correction was computed using the latest GOT ocean tide model GOT4.10 model. The solid earth tide correction and the pole tide correction were calculated using the same methods as those for the HY-2A IGDR and the Jason-2 GDR. The dynamic atmosphere correction was computed directly using the dynamic atmosphere correction (DAC) data derived from archiving, validation and interpretation of satellite oceanographic data (AVISO). Both the inverted barometer correction and the high frequency wind and pressure correction are included in the DAC data.

The range and geophysical corrections in the Jason-2 GDR are of good quality. Therefore, we validate the methods of the range and geophysical corrections used to reprocess HY-2A altimeter data by applying these methods to reprocess the Jason-2 range and geophysical corrections and comparing the results with the range and geophysical corrections in the Jason-2 GDR products. We then evaluated the accuracy of the reprocessed SSH measurements using the crossover analysis for single HY-2A mission and the crossover analysis between HY-2A and Jason-2 respectively. The performance of the reprocessed HY-2A SSH measurements is significantly improved with respect to the SSH measurements derived from the HY-2A IGDR product.

The El Niño Southern Oscillation (ENSO), which includes El Niño and La Niña, is a hot topic due to its huge impact on society. The ENSO originates from air-sea interactions and causes anomalies in a sea surface temperature and a sea level. The 2015–2016 El Niño has been the strongest El Niño event since 1997–1998. The radar altimeter can be used to monitor the El Niño through the sea level anomaly, which is the difference between the instantaneous sea surface height and the mean sea surface. We computed the sea level anomalies using the reprocessed HY-2A IGDR data from January 2015 to August 2016. The results show that the sea level anomalies derived from the HY-2A altimeter can observe the 2015–2016 El Niño well. This is the first application of the HY-2A SSH data in the ocean dynamics.

2 Validation of the methods of range and geophysical corrections

The sea surface height derived from the altimeter can be applied to observing the global sea level and its variation with time. The accuracy of the sea surface height measurements is directly linked with the accuracy of the corrections applied to deriving the sea surface height (Andersen and Scharroo, 2011).

The sea surface height (H_{ss}) derived from the altimeter can be expressed as

$$H_{ss} = H - (R + \Delta R_{co}), \tag{1}$$

$$R = R_{tr} + \Delta R_{ep} + \Delta R_{Do} + \Delta R_{sb} + \Delta R_{mo}, \tag{2}$$

$$\Delta R_{co} = \Delta R_{dr} + \Delta R_{we} + \Delta R_{io} + \Delta R_{ssb} + \Delta R_{oc} + \Delta R_{so} + \Delta R_{po} + \Delta R_{dac}, \tag{3}$$

where H is the height of the satellite above the reference ellipsoid; R is the range between the satellite and the sea surface corrected for instrumental effects; R_{tr} is the raw range obtained from onboard adaptive tracker; ΔR_{ep} is the epoch derived from 20 Hz waveform retracking; ΔR_{Do} is the Doppler correction derived from range rate; ΔR_{sb} is a system bias; ΔR_{mo} is the modeled instrumental correction; ΔR_{dr} is the dry troposphere correction; ΔR_{we} is the wet troposphere correction; ΔR_{io} is the ionosphere correction; ΔR_{ssb} is the sea state bias correction; ΔR_{oc} is the geocentric ocean tide correction (including the loading tide correction); ΔR_{so} is the solid earth tide correction; ΔR_{po} is the pole tide correction; and ΔR_{dac} is the dynamical atmospheric correction.

The eight corrections in Eq. (3) can fall into two groups. The former four are the range corrections while the latter four are the geophysical corrections. The range corrections deal with the corrections for the electromagnetic wave propagation velocity in non-vacuum environment and the scattering of the radar pulse from the non-Gaussian sea surface. The geophysical corrections remove the effects of the tidal height variations and the sea surface's response to the atmospheric pressure and wind from the sea surface height measurements.

In order to validate the methods of the range and geophysical corrections used to reprocess HY-2A altimeter data, we reprocessed the Jason-2 range and geophysical corrections using the same methods to reprocess HY-2A altimeter data and compared our results with the corresponding range and geophysical corrections in Jason-2 GDR. We used the version "D" of Jason-2 GDR, which has been fully calibrated and proved to have high accuracy in measuring the sea surface height. The HY-2A S-IGDR and Jason-2 GDR data span from June 1, 2014 to June 14, 2014 (one repeat cycle of HY-2A).

2.1 *Range correction*

2.1.1 *Sea state bias correction*

The sea state bias consists of the electromagnetic bias and the skewness bias. The electromagnetic bias is related to the fact that the wave troughs reflect more radar energy than the wave crests (Elfouhaily et al., 2000, 2001). The skewness bias is related to the fact that the altimeter uses a median tracker rather than a mean tracker (Andersen and Scharroo, 2011). Owing to the improvement of the precision orbit determination technology and other error corrections, the sea state bias has become the dominant source of error in satellite altimetry (Tran et al., 2006).

Theoretical SSB models by far are not practical. All the operational SSB models are empirical models. Conventional empirical SSB models are based on the wind speed and the significant wave height because these two parameters can be measured by the altimeter directly (Chelton, 1994; Gaspar and Florens, 1998; Gaspar et al., 2002; Labroue et al., 2004; Tran et al., 2010a). We call these models two-dimensional (2-D) SSB models. Tran et al. (2010b) presented a three-dimensional (3-D) SSB model using the sea level anomalies. In addition to the wind speed (U) and the significant wave height (SWH), Tran et al. (2010b) estimated the mean wave period (MWP) from a numerical wind wave model, NOAA's WaveWatch3 (NWW3). Jiang et al. (2016) analyzed the relationship between the electromagnetic bias and the wave period using the fourth order Stokes theory, which laid a foundation for introducing the mean wave period to develop a 3-D SSB model. In addition, Jiang et al. (2016) presented a 3-D SSB model developed using the crossover differences derived from the Jason-2 altimeter. Unlike Tran et al. (2010b), Jiang et al. (2016) used the mean wave period from the ECMWF reanalysis ERA-interim. Evaluated by the data from 2009 to 2011, the 3-D SSB estimates can increase the explained variance by 1.32 cm^2, or 1.15 cm in the RMS with respect to the 2-D SSB estimates. In this paper, we developed HY-2A 2-D and 3-D SSB models using Cycles 42–56 of the HY-2A IGDR data.

The wind speed and the significant wave height used to develop the SSB models are usually derived from the altimeter observations. However, the wind speed in the HY-2A IGDR is not reliable (the backscattering coefficient used to derive the wind speed in the HY-2A IGDR has not been fully calibrated, after the backscattering coefficient is fully calibrated, the wind speed will be better), so we used the wind speed derived from the ERA-interim to estimate the SSB for the HY-2A altimeter. Therefore, the significant wave height we used is derived from the HY-2A IGDR while the wind speed and the mean wave period are from the ERA-interim. The SSB estimates are based on a lookup table. The SSB estimate value for each grid in the lookup table is calculated using a nonparametric estimation method. The SSB estimates along the ground track can be obtained using the lookup table based on the wind speed, the SWH and the MWP. The data from ERA-Interim reanalysis is only available at 00:00, 06:00, 12:00, and 18:00 UTC every day in the form of a grid, so we have to interpolate the data onto the altimeter ground track locations. In this study, a bilinear interpolation is used in space and a linear interpolation is used in time.

The 2-D SSB estimates based on the wind speed and the SWH are presented as a 2-D lookup table and the ranges of the wind speed and the SWH are respectively 0–30 m/s and 0–12 m. The 2-D SSB estimates obtained from the HY-2A altimeter are shown in Fig. 1 in the form of 2-D grids with contours given in centimetre, while Fig. 2 shows the corresponding results derived from the Jason-2 altimeter. Shaded areas represent data density: (dark gray) holding no data, (red) when it is between 5 and 30 samples, (yellow) when it is between 30 and 100 samples, and (white) when it is larger than 100 samples. The SSB models derived from different altimeters are not identical because of differences in instrument design and waveform processing that is instrument dependent (Bao et al., 2015). As shown in Figs 1 and 2, the magnitude of the 2-D SSB estimates derived from the HY-2A altimeter is larger than that derived from the Jason-2 altimeter on the whole. However, the magnitudes of the SSB estimates de-

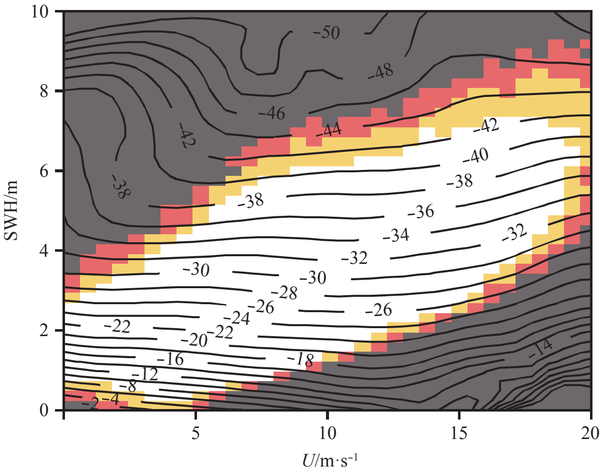

Fig. 1. HY-2A SSB estimates (in cm) obtained using a 2-D SSB model based on wind speed and SWH.

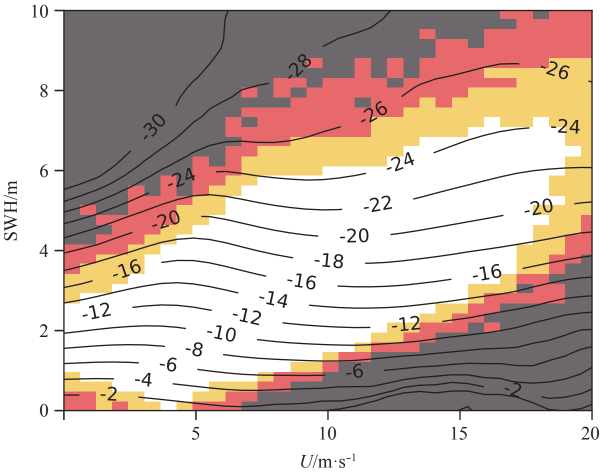

Fig. 2. Jason-2 SSB estimates (in cm) obtained using a 2-D SSB model based on wind speed and SWH.

rived from the two altimeters both increase with the SWH when the wind speed is fixed. For a given SWH, the magnitudes of the SSB estimates first increase with the wind speed and then decrease at higher wind speeds.

Similar to the 2-D SSB estimates, the 3-D SSB estimates based on the wind speed, the SWH and the MWP are presented as a 3-D lookup table and the ranges of the wind speed, the SWH and the MWP are respectively 0–30 m/s, 0–12 m and 0–18 s. In order to better represent the 3-D SSB estimates, we present the 3-D SSB estimates in the form of 2-D arrays by fixing the third parameter. Contours of the SSB estimates are displayed in centimetre and shown in Figs 3 and 4. Shaded areas also represent the data density: (dark gray) holding no data, (red) when it is between 1 and 5 samples, (yellow) when it is between 5 and 10 samples, and (white) when it is larger than 10 samples. Figures 3 and 4 show the 3-D SSB estimates derived from the HY-2A and Jason-2 altimeters respectively. The fixed values are near the mean values to ensure that there are enough measurements. As described in Jiang et al. (2016), the mean values of the MWP, the wind speed and the SWH are respectively around the MWP being 9 s, the wind speed being 7.5 m and the SWH being 2.5 m. Figures 3a and 4a agree closely with Figs 1 and 2. When the wind speed and the MWP are fixed, the magnitude of the SSB estimates is an increasing function of the SWH. In contrast, as shown in Figs 3b and 4b the magnitude of the SSB estimates is a decreasing function of the MWP when the wind speed and the SWH are fixed. In the data-rich region, there is an approximately 4 cm variation versus the MWP, with the magnitude of the SSB estimates decreasing as the wave period increases. As shown in Figs 3c and 4c, when the SWH is fixed, a variation with the MWP is more obvious than that with the wind speed in the data-rich region. For a given wind speed, the magnitude of the SSB estimates is a decreasing function of the MWP.

We first used the explained variance to evaluate the HY-2A 3-D SSB estimates. The explained variance is a main criterion to assess the quality of a SSB model. It is the reduction of the variance of the SSH differences obtained after applying the corresponding SSB corrections (Gaspar et al., 1994; Gaspar and Florens, 1998). In general, the lager the explained variance is, the better the SSB model is. The global crossover data from Cycles 42 to 56 were first used to calculate the explained variances. The variances explained by the 3-D SSB estimates, the 2-D SSB estimates and the SSB corrections in the HY-2A IGDR are 29.95, 28.23 and 26.47 cm^2, respectively. Therefore, compared with the 2-D SSB estimates and the SSB corrections in the HY-2A IGDR, the 3-D SSB estimates can increase the explained variances by 1.72 and 3.48 cm^2, or 1.31 and 1.87 cm RMS respectively.

We then binned the crossover data into 10° latitude bands and compute the explained variance in each band. We removed the data above the latitude of 60°S and 60°N for sea ice effects. The explained variances in comparison with the 1-D (–3.8% SWH) SSB model are given in Fig. 5. Obviously, compared with

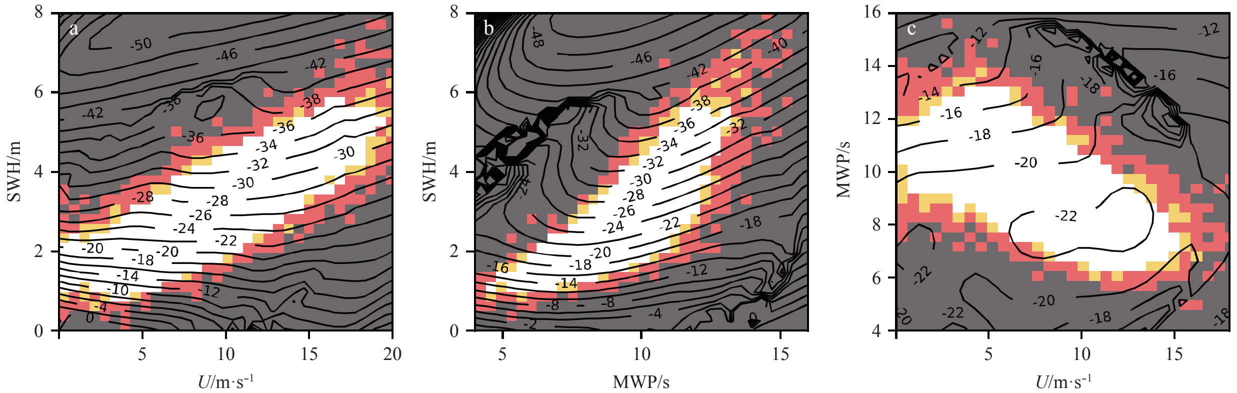

Fig. 3. HY-2A SSB estimates (in cm) obtained using a 3-D SSB model based on wind speed (a), SWH (b) and MWP (c).

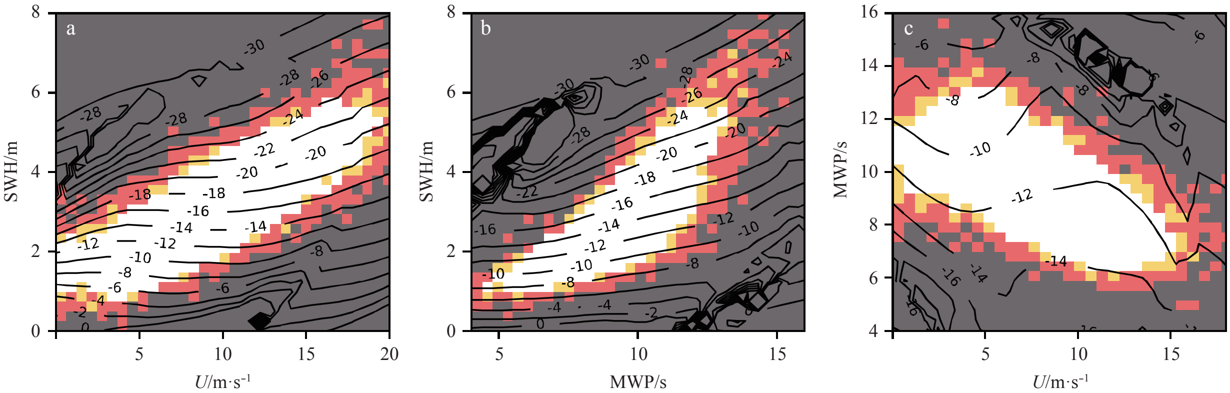

Fig. 4. Jason-2 SSB estimates (in cm) obtained using a 3-D SSB model based on wind speed (a), SWH (b) and MWP (c).

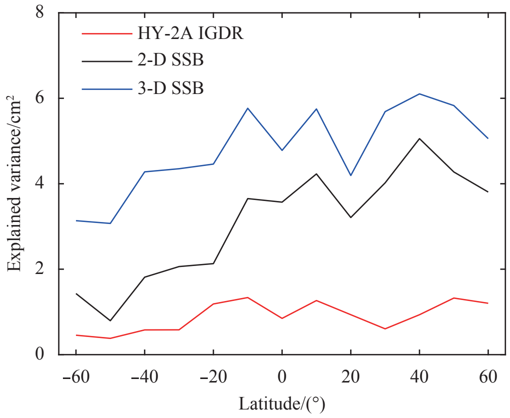

Fig. 5. Latitude distribution of the variance explained by 3-D SSB estimates and 2-D SSB estimates respectively in comparison with a 1-D (-3.8% SWH) benchmark. The variance explained by the SSB corrections in the HY-2A IGDR data is also given for comparison.

the 2-D SSB estimates and the SSB corrections in the HY-2A IGDR, the 3-D SSB estimates are better in all latitude regions. The improvement from the 2-D SSB estimates to the 3-D SSB estimates is especially obvious in the Southern Hemisphere.

Single-satellite SSH differences at the crossover points are the main tool to analyze the whole altimetry system performance (Ablain et al., 2010; Dorandeu et al., 2004; Prandi et al., 2015). They allow us to analyze the SSH consistency between the ascending and descending passes. The standard deviation of the crossover differences generally gives the main mission performance indicator. Figure 6 shows the standard deviation (STD) of the crossover SSH differences after using different SSB corrections. The results are obtained from the valid data set cycle per cycle. Obviously, compared with the 2-D SSB estimates and the SSB corrections in the HY-2A IGDR, the 3-D SSB estimates can significantly reduce the STD of the crossover SSH differences.

An along-track analysis is also usually used to assess the altimeter system performance by computing the sea level anomalies (SLAs) (Ablain et al., 2010; Dorandeu et al., 2004; Prandi et al., 2015). The analysis of the SLA is another indicator to estimate the performance of an altimetry system. It allows us to study the evolution of the SLA standard deviation, which can be used to monitor the long-term stability of the performance of an altimetry system. The along-track SLA is computed the along-track by subtracting the mean sea surface (MSS) from the instantaneous SSH measurements. The SLA standard deviation gives an estimate of the errors of the system. We used the CNES-CLS11 mean sea surface model to compute the along-track mean sea surface in this paper. The CNES-CLS11 model is computed from 16 a (1993–2009) of satellite altimetry data from a variety of missions (Schaeffer et al., 2012). Figure 7 shows the STD of the along-track SLAs after using different SSB corrections. Similarly, compared with the 2-D SSB estimates and the SSB corrections in the HY-2A IGDR, the 3-D SSB estimates can reduce the STD of the along-track SLAs.

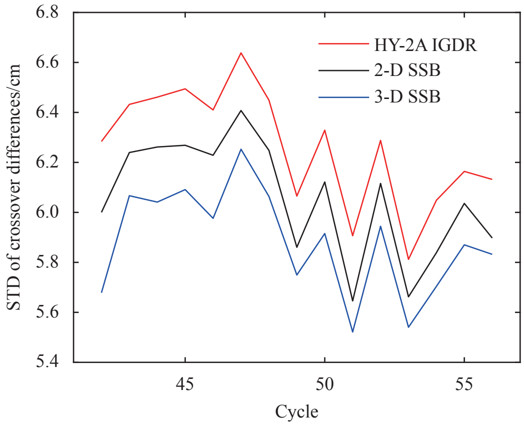

Fig. 6. The STD of the crossover SSH differences after using the 3-D SSB estimates, the 2-D SSB estimates and the SSB corrections in the HY-2A IGDR data, respectively.

Compared with the conventional 2-D SSB estimates based on the wind speed and the SWH, the 3-D SSB estimates can significantly increase the explained variance and reduce the STD of the crossover SSH differences and the STD of the along-track SLAs. Therefore, the 3-D SSB estimates can improve the accuracy of the SSH measurements and we used the 3-D SSB estimates to reprocess the sea sate bias correction for the HY-2A altimeter.

2.1.2 *Dry troposphere correction*

The dry troposphere correction is a correction for refraction from dry atmospheric gases and now it is the largest correction that should be added to the range measurements. The dry troposphere correction varies from 225 cm to 235 cm and its variation with time and space is very small (Andersen and Scharroo, 2011). The pressure can largely affect the vertical integration of the air

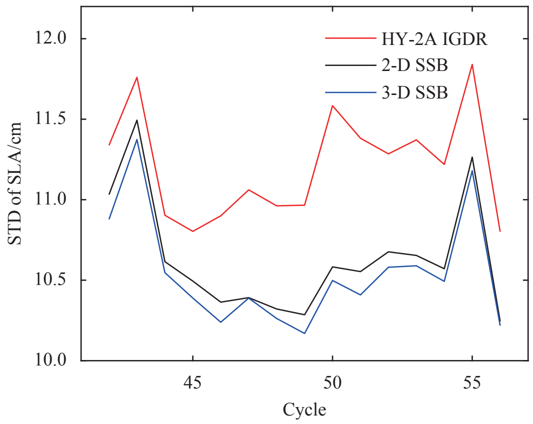

Fig. 7. The STD of the along-track SLAs after using 3-D SSB estimates, 2-D SSB estimates and the SSB corrections in HY-2A IGDR data, respectively.

density and the atmospheric pressure at the sea level can be used to derive the dry troposphere correction. The dry troposphere correction can be approximated by (Fu and Cazenave, 2001)

$$\Delta R_{\mathrm{dr}} \approx 0.227\,7 P_0 (1+0.002\,6\cos 2\varphi), \tag{4}$$

where P_0 is the sea level pressure and φ is the latitude. There is no direct way to measure the nadir sea level pressure from a satellite. In the Jason-2 GDR, the sea level pressure is derived from the operational ECMWF atmospheric model. However, due to several improvements in the processing, this model is not homogenous over the altimetry period (from 1993 onwards), especially in the first altimetry decade. ERA-interim provides better dry and wet troposphere corrections for the altimeter sea level at climate scales with respect to the operational ECMWF atmospheric model (Legeais et al., 2014; Carrère et al., 2016), and has been applied to the climate change initiative (CCI) project (Ablain et al., 2015). In this paper, we used the sea level pressure from the ECMWF reanalysis ERA-interim to calculate the dry troposphere correction.

As shown in Fig. 8, the reprocessed dry troposphere correction (Re-Model-Dry-Tropo) agrees well with the dry troposphere correction in Jason-2 GDR (GDR-Model-Dry-Tropo). The correlation coefficient (R) is close to 1 and the standard deviation of the differences between the reprocessed and GDR dry troposphere corrections is around 0.11 cm.

2.1.3 *Wet troposphere correction*

The wet troposphere correction is a correction for refraction-related water vapor and cloud liquid water droplets in the troposphere. The wet troposphere correction is mainly determined by the water vapor because correction for the cloud liquid water droplets is generally smaller than 1 cm (Fu and Cazenave, 2001). The wet troposphere correction varies from several millimeters in dry and cold air to more than 30 cm in hot and wet air (Andersen and Scharroo, 2011). The magnitude of the wet troposphere correction is much smaller than that of the dry troposphere correction. However, the wet troposphere correction is more complex due to higher temporal and spatial variations.

The wet troposphere correction owing to the cloud liquid water droplets (Fu and Cazenave, 2001) can be parameterized as

$$\Delta R_{\mathrm{li}} \approx 1.6 L_z, \tag{5}$$

$$L_z = \int_0^R \rho_{\mathrm{li}}(z)\,\mathrm{d}z, \tag{6}$$

where $\rho_{\mathrm{li}}(z)$ is the liquid water droplet density; R is the range between the satellite and the sea surface; L_z is the integrated columnar liquid water.

The water vapor range correction can be approximated by Fu and Cazenave (2001):

$$\Delta R_{\mathrm{vap}} = \frac{\beta'_{\mathrm{vap}}}{T_{\mathrm{eff}}} \int_0^R \rho_{\mathrm{vap}}(z)\,\mathrm{d}z, \tag{7}$$

where $\beta'_{\mathrm{vap}} = 1\,720\ \mathrm{K/(cm^3 \cdot g)}$ and T_{eff} is the effective temperature.

The vertical integral of water vapor and cloud liquid water can be obtained from a passive microwave radiometer. The Jason-2 advance microwave radiometer (AMR) measures the brightness temperatures in the nadir path at 18.7, 23.8 and 34 GHz. The atmosphere correction microwave radiometer (ACMR) onboard the HY-2A is a three-band microwave radiometer which measures radiation from atmosphere and earth's surface at 18.7, 23.8 and 37 GHz.

In this paper, the reprocessed wet troposphere correction is derived from the ACMR (Zhang et al., 2015). We used the wet troposphere correction calculated using the data from the ECMWF reanalysis ERA-interim to evaluate the wet troposphere correction derived from the ACMR. Figure 9 shows the comparison

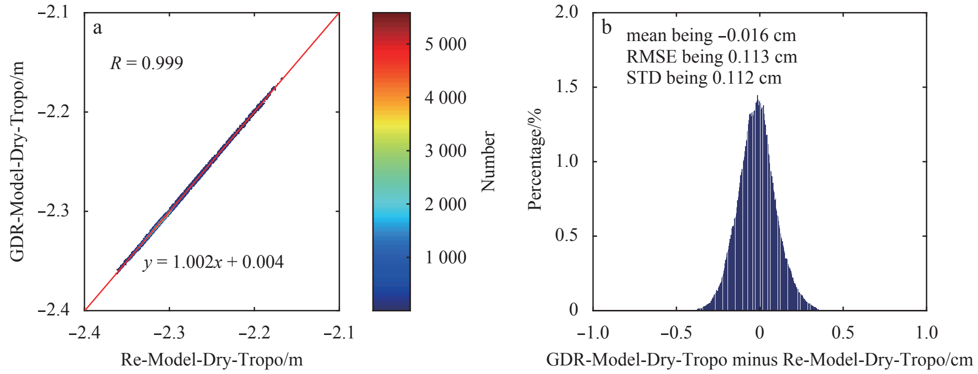

Fig. 8. Comparison between the reprocessed and GDR dry troposphere corrections: scatterplot (a), and difference distribution histogram between the two corrections (b).

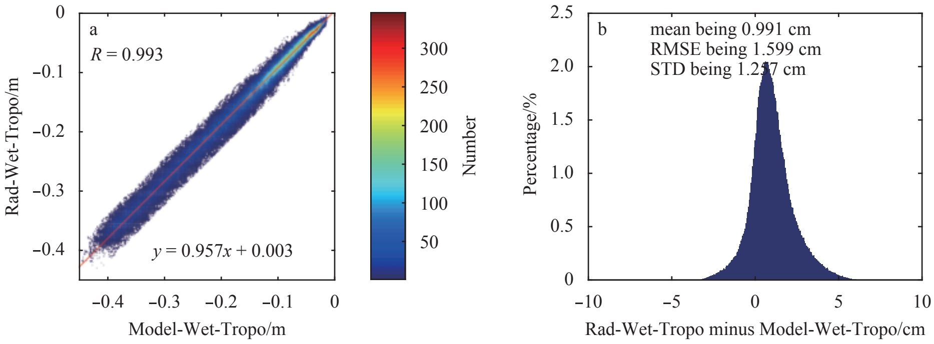

Fig. 9. Comparison between the wet troposphere corrections derived from AMR and ECMWF model: scatterplot (a) and difference distribution histogram between the two corrections (b).

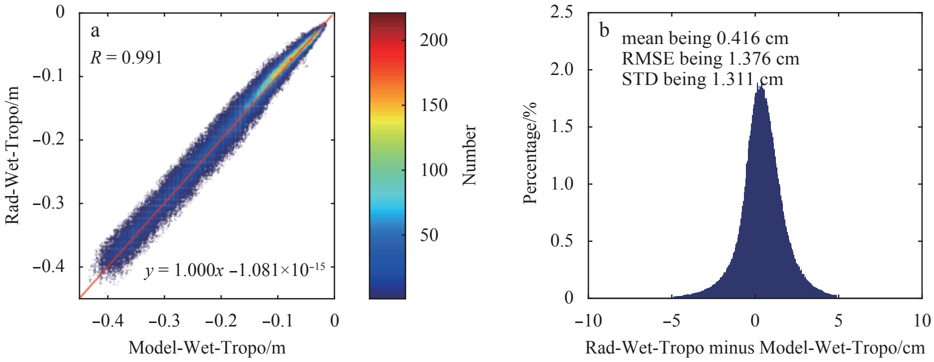

Fig. 10. Comparison between the wet troposphere corrections derived from ACMR and ECMWF model: scatterplot (a) and difference distribution histogram between the two corrections (b).

between the AMR and ERA-interim model wet troposphere corrections while Fig. 10 shows the comparison between the ACMR and ERA-interim model wet troposphere corrections. The wet troposphere correction derived from the ACMR is consistent with that derived from the ERA-interim.

2.1.4 *Ionosphere correction*

The ionosphere correction is a correction for the refraction of the electromagnetic wave due to the presence of free electrons in the ionosphere. The interaction between the electromagnetic wave and the electrons can slow down the electromagnetic wave. The total delay due to the refraction of the free electrons is proportion to the number of the free electrons per unit area from the sea surface to the altimeter. The ionosphere correction (Andersen and Scharroo, 2011) can be written as

$$\Delta R_{\mathrm{io}} = \frac{-k \cdot c_{\mathrm{te}}}{f^2}, \tag{8}$$

where c_{te} is the total electron content; k is a constant of 0.402 50× $10^{-16}\mathrm{GHz}^2\cdot\mathrm{m}^3/\mathrm{e}$; f is the electromagnetic radiation frequency.

The Jason-2 altimeter is a dual-frequency radar altimeter with the Ku-band and C-band frequencies of 13.6 and 5.3 GHz. The HY-2A altimeter is also a dual-frequency radar altimeter with the Ku-band and C-band frequencies of 13.58 and 5.25 GHz. The range measurements at C-band are less precise than that at Ku-band. The differences between the Ku-band and C-band measurements can be used to derive the ionosphere correction (Imel, 1994):

$$\Delta R_{\mathrm{io}} = \delta_{f_{\mathrm{Ku}}} \cdot (R_{\mathrm{Ku}} + b_{\mathrm{ss,Ku}} - R_{\mathrm{C}} - b_{\mathrm{ss,C}}), \tag{9}$$

$$\delta_{f_{\mathrm{Ku}}} = \frac{f_{\mathrm{Ku}}^2}{f_{\mathrm{Ku}}^2 - f_{\mathrm{C}}^2}, \tag{10}$$

where f_{Ku} and f_{C} are the electromagnetic radiation frequencies at Ku-band and C-band respectively. R_{Ku} and R_{C} are the range measurements at Ku-band and C-band respectively; and $b_{\mathrm{ss,\ Ku}}$ and $b_{\mathrm{ss,\ C}}$ are the sea state bias estimates at Ku-band and C-band respectively.

In the Jason-2 GDR, the ionosphere correction using the GIM model is provided. The GIM-derived ionosphere correction comes close to the ionosphere correction derived from the dual-frequency altimeter (Komjathy et al., 2005; Tseng et al., 2010). Figure 11 shows the comparison between the dual-frequency ionosphere correction in the HY-2A IGDR and the GIM ionosphere correction. We can see that the dual-frequency ionosphere correction in the HY-2A IGDR is of poor quality. We reprocessed the HY-2A dual-frequency ionosphere correction by correcting the C-band time tag bias of the HY-2A altimeter. Details of the method can been found in Jiang et al. (2017). Figure 12 shows the comparison between the reprocessed HY-2A dual-frequency ionosphere correction and the GIM ionosphere correction. The performance of the reprocessed HY-2A dual-frequency ionosphere correction is significantly improved with respect to the dual-frequency ionosphere correction in HY-2A IGDR products. Figure 13 shows the comparison between the Jason-2 dual-frequency ionosphere corrections and the GIM ionosphere corrections. The standard deviation of the differences between the dual-frequency and GIM ionosphere corrections for the Jason-2 is around 0.83 cm while that for the HY-2A is around 0.82

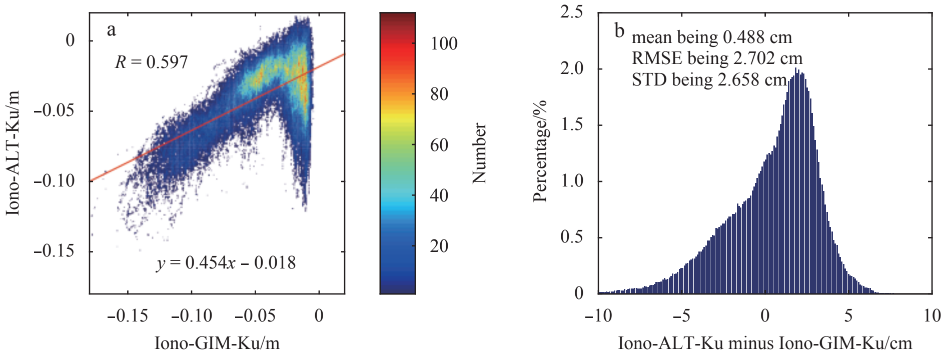

Fig. 11. Comparison between the HY-2A dual-frequency ionosphere corrections in HY-2A IGDR and GIM ionosphere corrections: scatterplot (a) and difference distribution histogram between the two corrections (b).

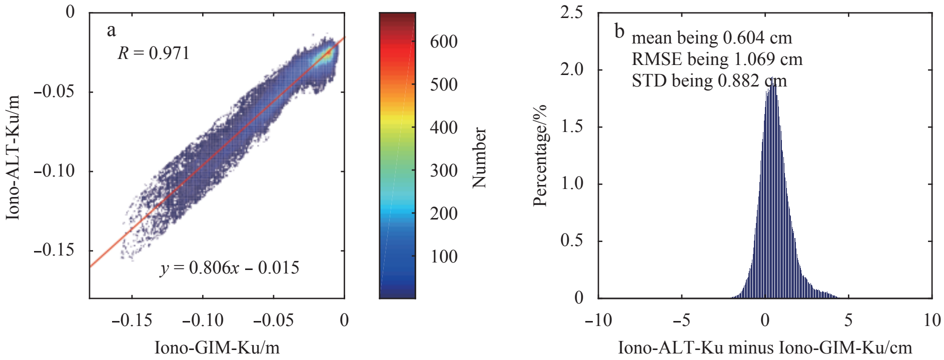

Fig. 12. Comparison between the reprocessed HY-2A dual-frequency ionosphere corrections and GIM ionosphere corrections: scatterplot (a) and difference distribution histogram between the two corrections (b).

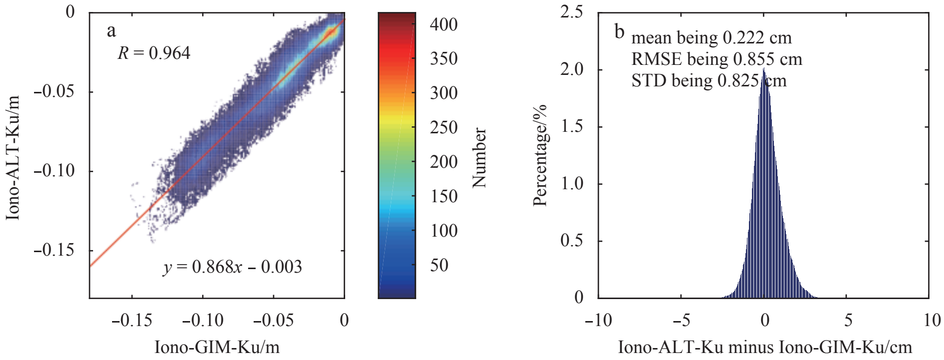

Fig. 13. Comparison between the Jason-2 dual-frequency ionosphere corrections and GIM ionosphere corrections: scatterplot (a) and difference distribution histogram between the two corrections (b).

cm. Therefore, the accuracy of the HY-2A dual-frequency ionosphere correction is almost the same as that of the Jason-2 dual-frequency ionosphere correction.

2.2 *Geophysical correction*

2.2.1 *Geocentric ocean tide correction*

Geocentric ocean tide is the sum of the ocean tide and the load tide. The ocean tide is caused by the solar and lunar gravity on the sea water of the earth's surface. The load tide is the deformation of the solid earth due to the periodic ocean tide load. The magnitude of the load tide is only 4%–6% of the ocean tide (Andersen and Scharroo, 2011).

Geocentric ocean tide correction is usually calculated using the global ocean tide models. A large number of the global ocean tide models, such as GOT (Andersen, 1995), FES (Ngodock et al., 2016), and TPXO (Egbert and Erofeeva, 2002), can be used to calculate the tide anywhere in the world at any time. In the Jason-2 GDR, the GOT4.8 and the FES2004 are used as the Solutions 1 and 2, respectively. The geocentric ocean tide is computed as the sum total of the diurnal and semidiurnal ocean and load tides, an equilibrium representation of the long-period ocean periods at all periods except the zero frequency term. In the HY-2A IGDR, the GOT00.2 is used as the Solution 1 geocentric ocean tide correction. In this paper, we used the latest GOT ocean tide model GOT4.10 to compute the geocentric ocean tide correction.

Figure 14 compares the reprocessed geocentric ocean tide (Re-Ocean-Tide) and the geocentric ocean tide (Solution1) in Jason-2 GDR (GDR-Ocean-Tide). The reprocessed geocentric ocean tide correction is close to the geocentric ocean tide correction in the Jason-2 GDR and the standard deviation of their differences is around 0.32 cm.

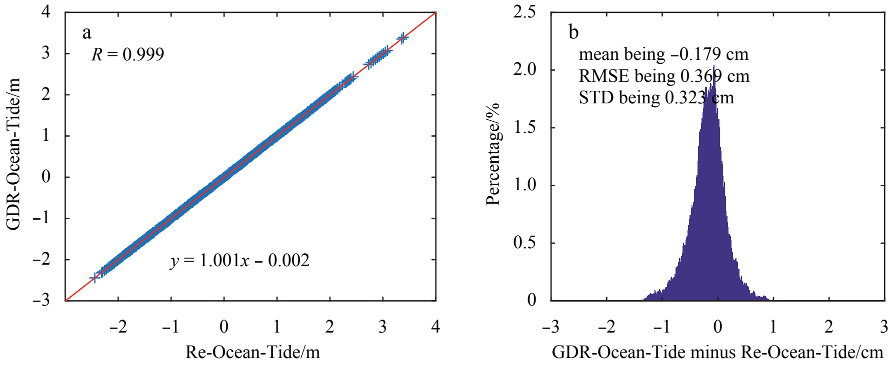

Fig. 14. Comparison between the reprocessed and GDR geocentric ocean tide corrections: scatterplot (a) and difference distribution histogram between the two corrections (b).

2.2.2 *Solid earth tide correction*

The solid earth tide correction is a correction for the response of the solid earth to the gravitational forces of the sun and the moon. The solid earth tide is determined by the Love numbers and can be computed using formulas described by Cartwright and Tayler (1971) and Cartwright and Edden (1973). The solid earth tide correction only processes temporal height variations, so the permanent part of the solid earth should be excluded. The magnitude of the solid earth tide correction reaches up to 20 cm with high accuracy.

As shown in Fig. 15, the maximum value of the differences between the reprocessed solid earth tide correction (Re-Solid-Earth-Tide) and the solid earth tide correction in the Jason-2 GDR (GDR-Solid-Earth-Tide) is less than 0.05 cm, which can be ignored in the SSH measurements.

2.2.3 *Pole tide correction*

The pole tide is the response of both the solid earth and the oceans to the centrifugal potential that is generated by small perturbations to the earth rotation axis. Modeling the pole tide requires the Love numbers, and a time series of perturbations to the earth's rotation axis, which can be measured with space technologies. The pole tide correction is computed using the formulas described by Wahr (1985):

$$\Delta R_{\mathrm{po}} = A\sin 2\varphi[(x-x_{\mathrm{avg}})\cos\lambda-(y-y_{\mathrm{avg}})\sin\lambda], \tag{11}$$

$$A=-\frac{\Omega^2R^2}{2g}\times\frac{\pi}{180\times360}\times(1+K_2)=-69.435\times10^{-3}, \tag{12}$$

where Ω is the nominal earth rotation angular velocity; R is the earth radius; K_2 is the Love number; φ and λ are the latitude and the longitude of the measurement, respectively; x and y are the nearest previous pole location data relative to the altimeter time; $x_{\mathrm{avg}}=0.042$, and $y_{\mathrm{avg}}=0.293$, are the mean pole position. In this paper, x and y are obtained from the International Earth Rotation and Reference Systems Service (IERS).

As shown in Fig. 16, the maximum value of the differences between the reprocessed pole tide correction (Re-Pole-Tide) and the pole tide correction in the Jason-2 GDR (GDR-Pole-Tide) can also be ignored in the SSH measurements.

2.2.4 *Dynamic atmosphere correction*

The dynamic atmosphere correction (DAC) contains an inverted barometer correction and the high frequency wind and pressure correction. As the atmospheric pressure increases and decreases, the sea surface tends to respond hydrostatically, falling or rising respectively. The correction for this effect is called the inverted barometer correction (Fu and Cazenave, 2001). In

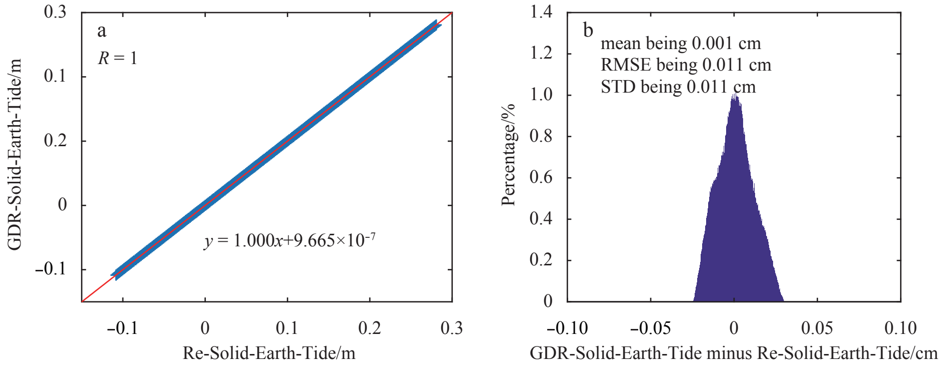

Fig. 15. Comparison between the reprocessed and GDR solid earth tide corrections: scatterplot (a) and difference distribution histogram between the two corrections (b).

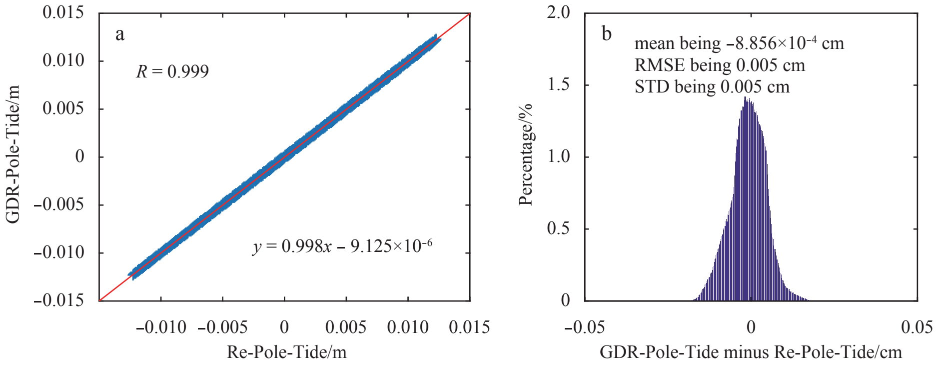

Fig. 16. Comparison between the reprocessed and GDR pole tide corrections: scatterplot (a) and difference distribution histogram between the two corrections (b).

general, 100 Pa increase in the atmospheric pressure can depress the sea surface by about 1 cm (Andersen and Scharroo, 2011). The high frequency wind and pressure correction is used to complement the inverted barometer correction. This correction is the difference between the response to the wind and the pressure minus the inverted barometer correction (Carrère and Lyard, 2003; Hirose et al., 2001; Pascual et al., 2008).

In the Jason-2 GDR, the inverted barometer correction and the high frequency wind and pressure correction are provided respectively. In the HY-2A IGDR product, the high frequency wind and pressure correction is invalid. In this paper, we used the DAC data obtained from the AVISO to reprocess the dynamic atmosphere correction. The DAC data from the AVISO contain both the inverted barometer correction and the high frequency wind and pressure correction. The DAC data are provided in the form of the latitude/longitude grids four times per day at 00:00, 06:00, 12:00 and 18:00 UTC. As shown in Fig. 17, the difference between the reprocessed dynamic atmosphere correction (Re-DAC) and the dynamic atmosphere correction in the Jason-2 GDR (GDR-DAC) can be ignored.

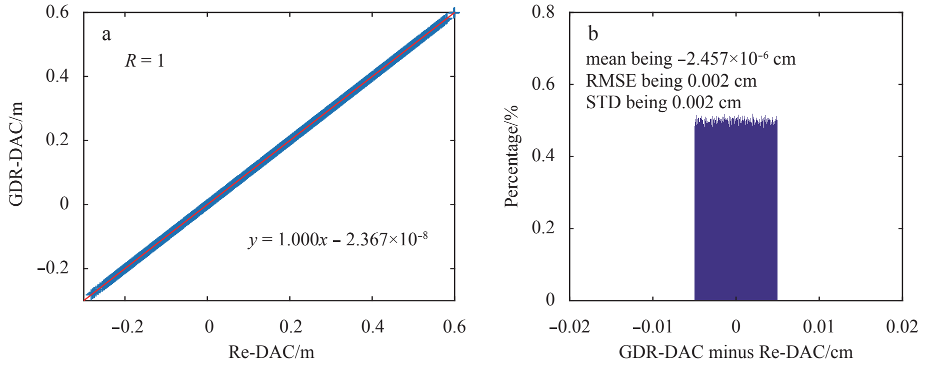

Fig. 17. Comparison between the reprocessed and GDR dynamic atmosphere corrections: scatterplot (a) and difference distribution histogram between the two corrections (b).

3 Assessment of reprocessed sea surface height measurements derived from HY-2A altimeter

The main objective of the altimeter is to derive the sea surface height. We first reprocessed the HY-2A IGDR data from June 1, 2014 to June 14, 2014 to compare the performance of the range and geophysical corrections we reprocessed with those in the HY-2A IGDR. The range and geophysical corrections we reprocessed and those in the HY-2A IGDR were respectively used to compute the sea surface height. We used crossover analysis to assess the accuracy of the reprocessed sea surface height measurements derived from the HY-2A altimeter. The crossover SSH difference is the main tool to assess the overall performance of satellite altimetry missions. When the crossovers are estimated from a single mission, the SSH differences provide information about the SSH consistency between ascending and descending tracks. When applied on two different missions, the SSH differences provide a relative SSH bias estimation and the drifts between two different missions (Prandi et al., 2015). To monitor the performances over stable surfaces, we only selected the data that satisfy the following criterions: (1) the bathymetry is lower than 1 000 m; (2) the SSH difference is lower than 20 cm; (3) the latitude is lower than 50°; and (4) the time difference is lower than 3 days.

The standard deviation of the SSH differences at crossovers is the main mission performance indicator. Figure 18 shows the histogram of the crossover SSH differences using the HY-2A IGDR data and reprocessed HY-2A IGDR data, respectively. The standard deviation of the crossover SSH differences using the reprocessed HY-2A IGDR data is about 6.12 cm, which is significantly lower than that (6.98 cm) using the HY-2A IGDR data. Therefore, the performance of the range and geophysical corrections we reprocessed is significantly improved with respect to those in HY-2A IGDR.

In order to further improve and assess the accuracy of the HY-2A SSH measurements, we reprocessed the HY-2A S-IGDR data. The Jason-2 altimeter has been proved to have high accuracy in

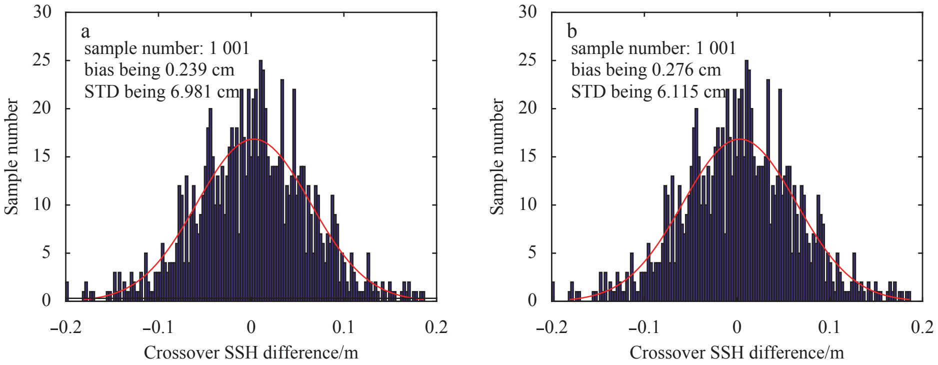

Fig. 18. Histogram of the crossover SSH differences for HY-2A altimeter using HY-2A IGDR data (a) and using reprocessed HY-2A IGDR data (b).

measuring the SSH. Therefore, we can assess the accuracy of the reprocessed HY-2A SSH measurements by cross-calibration with the Jason-2. We retracked the waveforms in the HY-2A S-IGDR and corrected the time tag bias. Table 2 presents the models and methods we used to reprocess the data for the HY-2A and the Jason-2. The orbit H and the tracker range R_{tr} for HY-2A are directly derived from the HY-2A S-IGDR. The MLE4 (Thibaut et al., 2010; Wang et al., 2013a, b) retracking algorithm was used to derive the epoch (tracker range offset) and the significant wave height. The Doppler correction is to correct the errors caused by the vertical component of the satellite velocity relative to the sea surface (Chelton et al., 1989). The system bias is the inherent SSH bias between the HY-2A and the Jason-2. The modeled instrumental correction for the instrumental point target response (PTR) bias is a correction computed to correct for differences between the modeled system response and the model inputs, and was computed using a lookup table (Thibaut et al., 2010). When comparing the performance of a mission with that of another mission, we should spend much attention to removing the contributions of ocean variability and geophysical corrections. The geophysical corrections for two missions should be identical. The same interpolation procedure should be used to compute the SSH at the crossovers and the cubic spline functions were used in this paper.

Table 2. Models and methods used to reprocess the data for HY-2A and Jason-2

	HY-2A reprocess	Jason-2 reprocess
Orbit	HY-2A S-IGDR	GDR-D
Tracker	HY-2A S-IGDR	GDR-D
Epoch	MLE4	GDR-D MLE4
Doppler correction	NSSC[1)]	GDR-D
System bias	NSSC[1)]	GDR-D
Modeled instrumental correction	NSSC[1)]	GDR-D
Dry troposphere correction	ERA-Interim model	ERA-Interim model
Wet troposphere correction	ACMR	AMR
Ionospheric correction	Improved dual frequency correction	Dual frequency correction
Sea state bias correction	3-D nonparametric SSB	3-D nonparametric SSB
Geocentric ocean tide correction	GOT4.10 model	GOT4.10 model
Solid earth tide correction	(Cartwright and Edden, 1973)	(Cartwright and Edden, 1973)
Pole tide correction	(Wahr, 1985)	(Wahr, 1985)
Dynamical atmospheric correction	DAC from AVISO	DAC from AVISO

Note: [1)] Determined using an algorithm from the National Space Science Center, Chinese Academy of Sciences.

Figure 19 shows the histogram of the crossover SSH differences for the HY-2A using the reprocessed HY-2A S-IGDR data. The standard deviation of the crossover SSH differences for the HY-2A is around 4.53 cm, which is significantly reduced with respect to the results in Fig. 18. Therefore, the retracking algorithm can significantly improve the accuracy of the HY-2A SSH measurements with respect to the retracking algorithm used in the HY-2A IGDR. Figure 20 presents the histogram of the SSH differences between the HY-2A and the Jason-2 (the mean value of the SSH differences has been removed). The standard deviation of the SSH differences is around 5.22 cm. As shown in Fig. 21 and Fig. 22, both the distribution of the crossover SSH differences for the HY-2A and the distribution of the SSH differences between the HY-2A and the Jason-2 have no obvious geographical relevance. Therefore, the systematic consistencies between ascending and descending passes are of good quality.

4 Application of HY-2A altimeter to observation of 2015-2016 El Niño

El Niño originates from air-sea interactions and can cause fluctuations in the sea surface temperature, and the associated sea level change. These temperature fluctuations only take place in the equatorial Pacific Ocean, and usually last several months. El Niño often happens with an irregular frequency anywhere between every two to seven years (Picaut et al., 2002). The presence of El Niño can greatly affect weather patterns and ocean

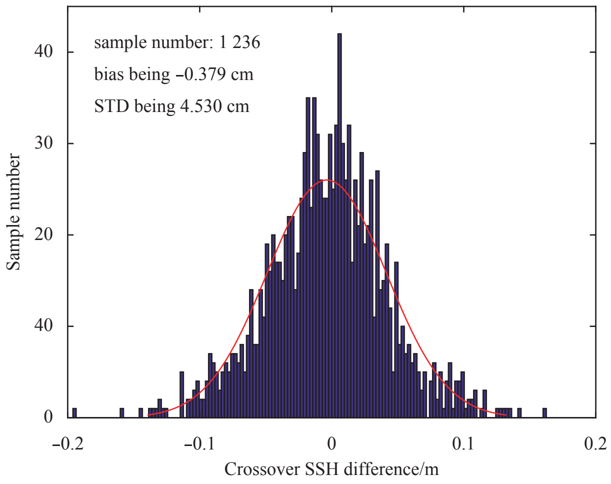

Fig. 19. Histogram of the crossover SSH differences for HY-2A using reprocessed HY-2A S-IGDR data.

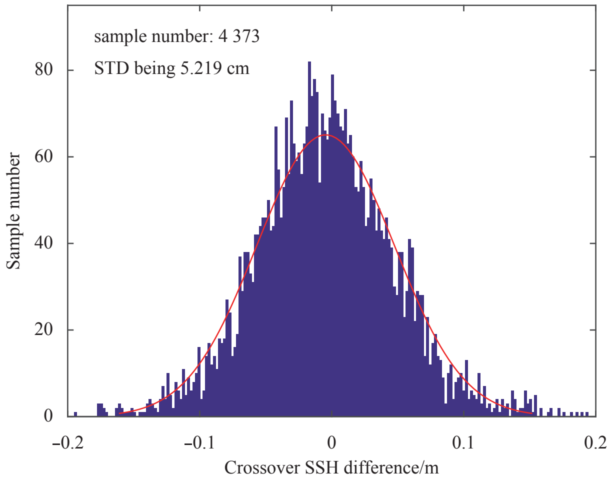

Fig. 20. Histogram of the SSH differences between HY-2A and Jason-2.

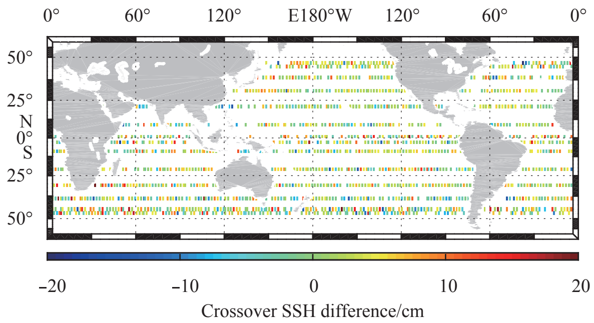

Fig. 21. Distribution of the crossover SSH differences for HY-2A using reprocessed HY-2A S-IGDR data.

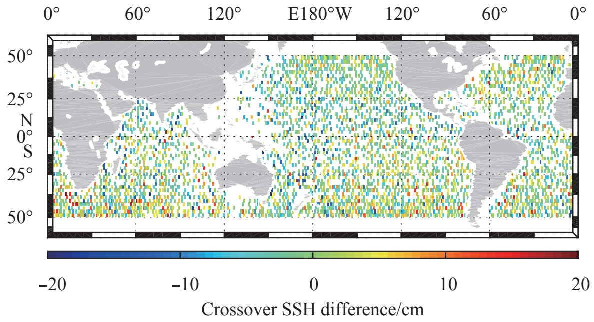

Fig. 22. Distribution of the crossover SSH differences between HY-2A and Jason-2.

conditions across large portions of the world for a long period of time.

Normally, the trade winds blow towards the west along the equator from South America to Asia in the tropical Pacific Ocean. These winds pile up warm surface water off Asia, so the sea level is higher at Indonesia than at Ecuador in South America. During the El Niño, the trade winds tend to lose strength even reverse and blow from west to east. Less water is pushed westward and, consequently, waters in the central and eastern Pacific Ocean begin to heat up. Therefore, the sea level is lower than normal in the western tropical Pacific Ocean and higher than normal in the eastern tropical Pacific Ocean (Picaut et al., 2002).

The sea level anomaly (SLA) is the difference between the instantaneous sea surface height and the mean sea surface (MSS, S_{ms}) and it can be applied to monitoring the El Niño (Chelton and Schlax, 1996; Delcroix et al., 1994; Picaut et al., 2002). We look at sea level anomaly because the total sea surface height measured by the altimeter varies from -100 to 100 m. Most of the sea surface height is constant. The sea level variations caused by the El Niño account for less than 1% of the total sea surface height. If the constant part of the sea surface height were not removed, the El Niño signal would not be observable. The sea level anomaly (A_{sl}) can be determined as

$$A_{sl} = H_{ss} - S_{ms}. \tag{13}$$

The temporal mean of the dynamic sea surface height can be removed by subtracting the mean sea surface height from the instantaneous sea surface height. The sea level anomalies have zero mean in principle. Sea surface height observations over a long time period are averaged and data from several repeat missions are combined to compute the mean sea surface height. There are a number of mean sea surface models and we used the CNES-CLS11 model in this paper.

The 2015–2016 El Niño has been the strongest El Niño events since 1997–1998. In this paper, we aimed at observing the 2015–2016 El Niño using the sea level anomalies derived from the HY-2A altimeter. We reprocessed the HY-2A IGDR data using the error correction methods described in this paper. The altimetry data from the HY-2A are centralized between 30°N and 30°S, with the largest focus on the equatorial region of the Pacific Ocean. Figure 23 presents the mean sea level anomalies over the tropical Pacific Ocean derived from the HY-2A altimeter. The along-track sea level anomalies over a month are mapped to a 1°×1° grid. In the winter of 2015, the sea level anomalies are obviously below 0 in the western tropical Pacific Ocean and positive in the eastern tropical Pacific Ocean, which means that the sea level is lower than normal in the western tropical Pacific Ocean and higher than normal in the eastern Pacific Ocean. From May 2015 to October 2015, the magnitudes of the sea level anomalies are gradually increasing, which means that the intensity of the El Niño is increasing with time. From October 2015 to December 2015, the phenomenon of El Niño is most obvious. After January

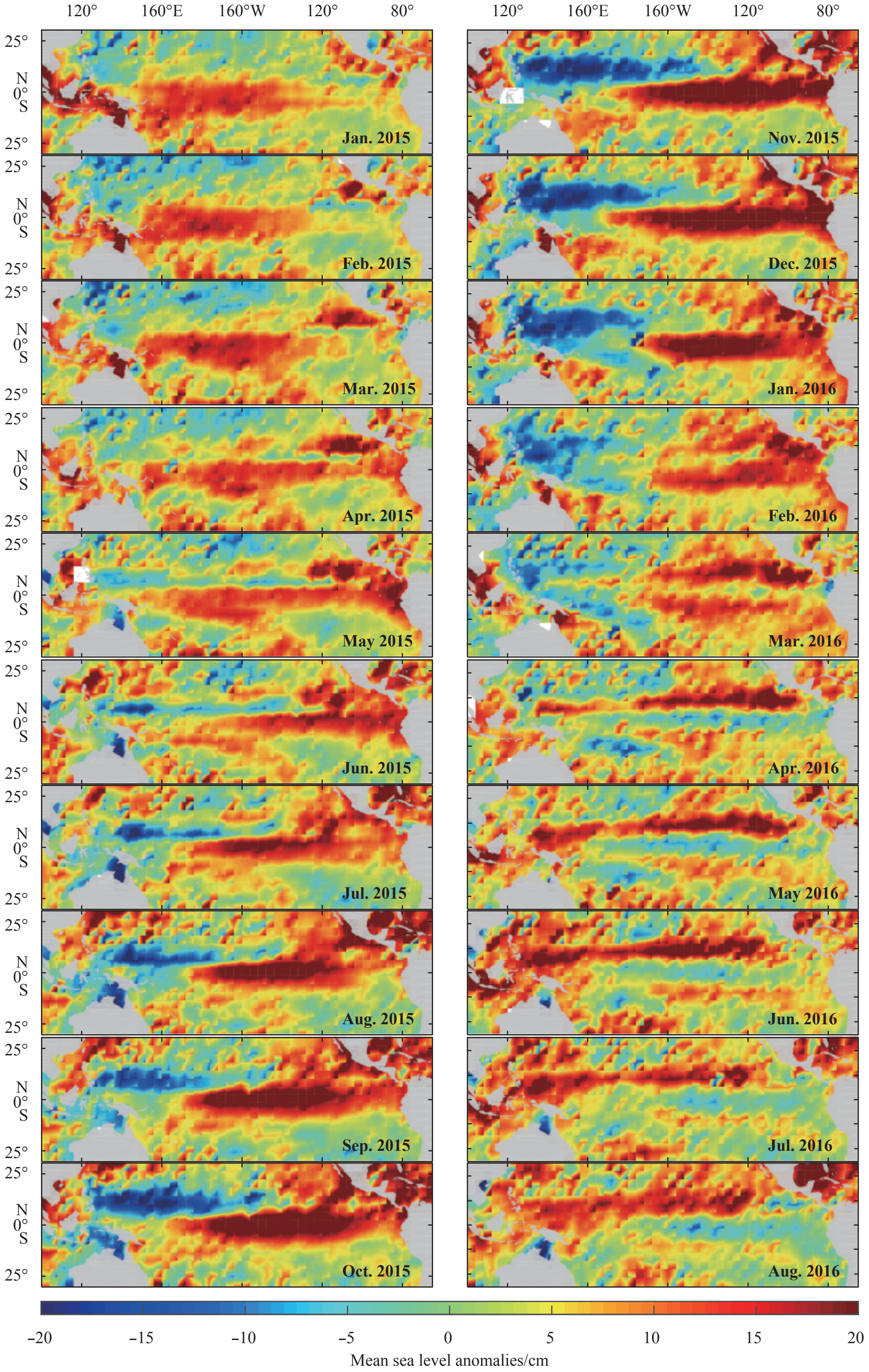

Fig. 23. Mean sea level anomalies (MSLA) over the tropical Pacific Ocean obtained from the HY-2A altimeter.

2016, the intensity of the El Niño gradually decreases. After April 2016, the sea level anomalies in some parts of the eastern tropical Pacific Ocean become negative while those in the western tropical Pacific Ocean become positive. Therefore, there is a trend that the El Niño turns to La Niña after April 2016.

5 Summary and conclusions

In this article, we assessed the reprocessed SSH measurements derived from the HY-2A IGDR and the S-IGDR, and applied the reprocessed sea level anomalies derived from the HY-2A IGDR to monitoring the 2015–2016 El Niño events.

The methods of the range and geophysical corrections we used to reprocess the HY-2A altimeter data were validated by using these methods to reprocess the Jason-2 range and geophysical corrections and comparing the results with the range and geophysical corrections in the Jason-2 GDR products. The results show that the reprocessed range and geophysical corrections are well consistent with the corresponding corrections in the Jason-2 GDR. The crossover analysis was used to evaluate the reprocessed SSH measurements. The performance of the reprocessed HY-2A SSH measurements is significantly improved with respect to the SSH measurements derived the HY-2A IGDR product. The reprocessed sea level anomalies obtained from the HY-2A altimeter were applied to observing the 2015–2016 El Niño events. Results show that the HY-2A altimeter can well observe the 2015–2016 El Niño.

Nowadays, the data from the HY-2A altimeter are mainly processed and evaluated in the open ocean. In the future, we will process the data in the costal, inland and ice sheet and compare the data with some other altimeters such as Jason-2, Cryosat-2 and Saral/Altika.

Acknowledgements

The Jason-2 GDR-D data and the DAC data are obtained from AVISO (ftp://avisoftp.cnes.fr). The mean wave period and the wind speed used to derive the SSB estimates of the HY-2A altimeter are downloaded from ECMWF reanalysis project ERA-interim (http://apps.ecmwf.int/datasets/data/interim-full-daily/). The data used to compute the pole tide correction are obtained from IERS (www.iers.org). The authors would like to express appreciation to AVISO, ECMWF and IERS for providing us with data. Besides, they express appreciation to NSOAS for providing us with HY-2A IGDR and S-IGDR data.

References

Ablain M, Cazenave A, Larnicol G, et al. 2015. Improved sea level record over the satellite altimetry era (1993–2010) from the Climate Change Initiative Project. Ocean Science, 11(1): 67–82

Ablain M, Philipps S, Picot N A, et al. 2010. Jason-2 global statistical assessment and cross-calibration with Jason-1. Marine Geodesy, 33(S1): 162–185

Andersen O B. 1995. Global ocean tides from ERS 1 and TOPEX/POSEIDON altimetry. Journal of Geophysical Research: Oceans, 100(C12): 25249–25259

Andersen O B, Scharroo R. 2011. Range and geophysical corrections in coastal regions: and implications for mean sea surface determination. In: Vignudelli S, Kostianoy A, Cipollini P, et al., eds. Coastal Altimetry. Berlin, Heidelberg: Springer, 103–145

Bao Lifeng, Gao Peng, Peng Hailong, et al. 2015. First accuracy assessment of the HY-2A altimeter sea surface height observations: cross-calibration results. Advances in Space Research, 55(1): 90–105

Carrère L, Faugère Y, Ablain M. 2016. Major improvement of altimetry sea level estimations using pressure-derived corrections based on ERA-Interim atmospheric reanalysis. Ocean Science, 12(3): 825–842

Carrère L, Lyard F. 2003. Modeling the barotropic response of the global ocean to atmospheric wind and pressure forcing-comparisons with observations. Geophysical Research Letters, 30(6): 225–242

Cartwright D E, Edden A C. 1973. Corrected tables of tidal harmonics. Geophysical Journal International, 33(3): 253–264

Cartwright D E, Tayler R J. 1971. New computations of tide-generating potential. Geophysical Journal International, 23(1): 45–73

Chelton D B. 1994. The sea-state bias in altimeter estimates of sea level from collinear analysis of Topex data. Journal of Geophysical Research: Oceans, 99(C12): 24995–25008

Chelton D B, Schlax M G. 1996. Global observations of oceanic Rossby waves. Science, 272(5259): 234–238

Chelton D B, Walsh E J, MacArthur J L. 1989. Pulse compression and sea level tracking in satellite altimetry. Journal of Atmospheric and Oceanic Technology, 6(3): 407–438

Delcroix T, Boulanger J P, Masia F, et al. 1994. Geosat-derived sea level and surface current anomalies in the equatorial Pacific during the 1986–1989 El Niño and La Niña. Journal of Geophysical Research: Oceans, 99(C12): 25093–25107

Dorandeu J, Ablain M, Faugère Y, et al. 2004. Jason-1 global statistical evaluation and performance assessment: calibration and cross-calibration results. Marine Geodesy, 27(3–4): 345–372

Egbert G D, Erofeeva S Y. 2002. Efficient inverse modeling of barotropic ocean tides. Journal of Atmospheric and Oceanic Technology, 19(2): 183–204

Elfouhaily T, Thompson D R, Chapron B, et al. 2000. Improved electromagnetic bias theory. Journal of Geophysical Research: Oceans, 105(C1): 1299–1310

Elfouhaily T, Thompson D R, Chapron B, et al. 2001. Improved electromagnetic bias theory: inclusion of hydrodynamic modulations. Journal of Geophysical Research: Oceans, 106(C3): 4655–4664

Fu L L, Cazenave A. 2001. Satellite Altimetry and Earth Sciences: A Handbook of Techniques and Applications. International Geophysical Series, Vol. 69. San Diego: Academic Press, 1–70

Gaspar P, Florens J P. 1998. Estimation of the sea state bias in radar altimeter measurements of sea level: results from a new nonparametric method. Journal of Geophysical Research: Oceans, 103(C8): 15803–15814

Gaspar P, Labroue S, Ogor F, et al. 2002. Improving nonparametric estimates of the sea state bias in radar altimeter measurements of sea level. Journal of Atmospheric and Oceanic Technology, 19(10): 1690–1707

Gaspar P, Ogor F, Le Traon P Y L, et al. 1994. Estimating the sea state bias of the Topex and Poseidon altimeters from crossover differences. Journal of Geophysical Research: Oceans, 99(C12): 24981–24994

Hirose N, Fukumori I, Zlotnicki V, et al. 2001. Modeling the high-frequency barotropic response of the ocean to atmospheric disturbances: sensitivity to forcing, topography, and friction. Journal of Geophysical Research: Oceans, 106(C12): 30987–30995

Imel D A. 1994. Evaluation of the Topex/Poseidon dual-frequency ionosphere correction. Journal of Geophysical Research: Oceans, 99(C12): 24895–24906

Jiang Maofei, Xu Ke, Liu Yalong, et al. 2016. Estimating the sea state bias of Jason-2 altimeter from crossover differences by using a three-dimensional nonparametric model. IEEE Journal of Selected Topics in Applied Earth Observations and Remote Sensing, 9(11): 5023–5043

Jiang Maofei, Xu Ke, Liu Yalong, et al. 2017. Estimating the time tag bias of HY-2A radar altimeter and its application to dual-frequency ionosphere correction. Marine Geodesy, 40(6): 361–377

Komjathy A, Sparks L, Wilson B D, et al. 2005. Automated daily processing of more than 1000 ground-based GPS receivers for studying intense ionospheric storms. Radio Science, 40(6): 1–11

Labroue S, Gaspar P, Dorandeu J, et al. 2004. Nonparametric estimates of the sea state bias for the Jason-1 radar altimeter. Marine Geodesy, 27(3–4): 453–481

Legeais L, Ablain M, Thao S. 2014. Evaluation of wet troposphere path delays from atmospheric reanalyses and radiometers and their impact on the altimeter sea level. Ocean Science, 10(6): 893–905

Naenna P. 2011. Numerical and analytical studies of the electromagnetic bias in satellite altimetry [dissertation]. Columbus: The Ohio State University

Ngodock H E, Souopgui I, Wallcraft A J, et al. 2016. On improving the accuracy of the M2 barotropic tides embedded in a high-resolution global ocean circulation model. Ocean Modelling, 97: 16–26

Pascual A, Marcos M, Gomis D. 2008. Comparing the sea level response to pressure and wind forcing of two barotropic models: validation with tide gauge and altimetry data. Journal of Geophysical Research: Oceans, 113(C7): 141–162

Peng Hailong, Lin Mingsen, Mu Bo, et al. 2015. Global statistical evaluation and performance analysis of HY-2A satellite radar altimeter data. Haiyang Xuebao (in Chinese), 37(7): 54–66

Picaut J, Hackert E, Busalacchi A J, et al. 2002. Mechanisms of the 1997–1998 El Niño-La Niña, as inferred from space-based observations. Journal of Geophysical Research: Oceans, 107(C5): 5–1–5–18

Prandi P, Philipps S, Pignot V, et al. 2015. SARAL/AltiKa global statistical assessment and cross-calibration with Jason-2. Marine Geodesy, 38(S1): 297–312

Schaeffer P, Faugére Y, Legeais J F, et al. 2012. The CNES_CLS11 global mean sea surface computed from 16 years of satellite altimeter data. Marine Geodesy, 35(S1): 3–19

Thibaut P, Poisson J C, Bronner E, et al. 2010. Relative performance of the MLE3 and MLE4 retracking algorithms on Jason-2 altimeter waveforms. Marine Geodesy, 33(S1): 317–335

Tran N, Labroue S, Philipps S, et al. 2010a. Overview and update of the sea state bias corrections for the Jason-2, Jason-1 and TOPEX missions. Marine Geodesy, 33(S1): 348–362

Tran N, Vandemark D, Chapron B, et al. 2006. New models for satellite altimeter sea state bias correction developed using global wave model data. Journal of Geophysical Research: Oceans, 111(C9): 141–152

Tran N, Vandemark D, Labroue S, et al. 2010b. Sea state bias in altimeter sea level estimates determined by combining wave model and satellite data. Journal of Geophysical Research: Oceans, 115(C3): C03020

Tseng K H, Shum C K, Yi Yuchan, et al. 2010. Regional validation of Jason-2 dual-frequency ionosphere delays. Marine Geodesy, 33(S1): 272–284

Wahr J M. 1985. Deformation induced by polar motion. Journal of Geophysical Research: Solid Earth, 90(11): 9363–9368

Wang Lei, Xu Ke, Liu Peng, et al. 2013a. An echo model for big antenna mispointing angle and its application in HY-2A radar altimeter. Acta Electronica Sinica (in Chinese), 41(9): 1836–1841

Wang Lei, Xu Ke, Xu Xiyu, et al. 2013b. A new method for computing radar altimeter look-up correction table and its application. Journal of Electronics and Information Technology (in Chinese), 35(4): 908–914

Zhang Dehai, Wang Zhenzhan, Li Yun, et al. 2015. Preliminary analysis of HY-2 ACMR data. In: Proceedings of 2015 IEEE International Geoscience and Remote Sensing Symposium. Milan, Italy: IEEE, 177–180

Zheng Gang, Yang Jingsong, Ren Lin. 2014. Retrieval models of water vapor and wet tropospheric path delay for the HY-2A calibration microwave radiometer. Journal of Atmospheric and Oceanic Technology, 31(7): 1516–1528